Tissue Harmonic Image Analysis Based on Spatial Covariance

Che-Chou Shen and Pai-Chi Li, *Senior Member, IEEE*

***Abstract*—The van Cittert-Zernike theorem has been widely used to describe spatial covariance of the pressure field backscattered from a speckle object. Spatial covariance contains important information in the context of correlation-based correction of sound velocity inhomogeneities. Previous work was primarily based on spatial covariance analysis for linear imaging. In this paper, we extend the analysis to tissue harmonic imaging. Specifically, we investigate effects of the signal-to-noise ratio (SNR) and sound velocity inhomogeneities on spatial covariance. Results from tissue harmonic imaging are also compared with those from linear imaging. Both simulations and experiments are performed. At high SNRs, although both linear imaging and tissue harmonic imaging have spatial covariance functions close to theory, the spatial covariance of tissue harmonic imaging is consistently lower than that of linear imaging regardless of the presence of sound velocity inhomogeneities. At low SNRs, on the other hand, spatial covariance of tissue harmonic imaging is significantly affected. Because the tissue harmonic signal is much weaker than the linear counterpart, the low SNR reduces the accuracy of correlation-based estimation. It is concluded that the linear signal is more suitable for correlation-based correction of sound velocity inhomogeneities, despite the fact that tissue harmonic imaging generally has improved image quality over linear imaging.**

I. INTRODUCTION

A MAJOR PROBLEM for diagnostic ultrasound systems is the image quality degradation resulting from sound velocity inhomogeneities [1]–[8]. Sound velocity inhomogeneities distort both amplitude and phase of the acoustic signal. Many methods have been proposed to restore the degraded resolution [3]–[8]. Flax and O'Donnell proposed that sound velocity inhomogeneities can be modeled as a near field phase screen. Under this assumption, the inhomogeneities simply produce time delay errors that can be estimated based on the correlation function of signals either from adjacent channels [3], [4] or from individual channels and the beam sum [5]. An alternative approach models sound velocity variations by a phase screen displaced from the transducer surface [6]. Hence, acoustic signals are backpropagated to an optimal depth before the correlation function is calculated. In the presence of distributed sound velocity inhomogeneities, the received signal can also be decomposed into spectral sub-bands before the time delays are estimated [7]. Although the specific details are different, all of the above methods utilize the correlation function to find time delay errors. Performance of the correlation-based methods is determined by spatial covariance: the higher the correlation, the more accurate the time delay estimates.

Spatial covariance is described by the van Cittert-Zernike theorem [9]. It has been shown that the spatial covariance of signals backscattered from randomly distributed scatterers and the incident pressure field are a Fourier pair. Consequently, spatial covariance decreases as the distance between two channels increases. Without focusing errors, spatial covariance is proportional to the autocorrelation function of the transmitting aperture. With focusing errors, on the other hand, the spatial covariance function becomes narrower because the transmit beam becomes wider.

Spatial covariance decreases with distance because of phase-sensitive interference of scatterers within a sample volume. The spatial decorrelation rate is determined by both the sample volume geometry and the carrier frequency. For a fixed sample volume, the decorrelation rate is proportional to frequency, because a higher frequency results in larger phase changes, assuming all other conditions are fixed. Similarly, for a fixed frequency, a larger sample volume also increases the spatial decorrelation rate. This leads to an important property of the van Cittert-Zernike theorem in linear imaging: spatial covariance is independent of the imaging frequency if a fixed aperture is used. In other words, although a high frequency results in a faster decorrelation rate, it also produces a smaller sample volume because the aperture is unchanged. Thus, the spatial covariance for linear imaging at f_0 is the same as the spatial covariance for linear imaging at $2f_0$ using the same aperture. This property will be tested and extended to tissue harmonic imaging in this paper.

Tissue harmonic imaging has proven to provide clinically useful images even on technically difficult bodies [10]–[14]. Because of its improved acoustic beam characteristics, it was suggested that the tissue harmonic signal can be combined with the linear signal to improve accuracy of correlation-based estimation of time delay errors [15]. In other words, by properly selecting the frequency pass bands of filters used for imaging and for time delay estimation, advantages over conventional approaches may be provided. To develop an optimal correction strategy successfully, it is necessary to understand characteristics of spatial covariance in tissue harmonic imaging fully. In this paper, spatial covariance of tissue harmonic signals is

Manuscript received October 25, 2000; accepted May 28, 2001. The work was supported by the National Science Council of the R.O.C. under Grant NSC 89-2320-B-002-152-M08.

The authors are with the Department of Electrical Engineering, National Taiwan University, Taipei, Taiwan, R.O.C. (e-mail: paichi@cc.ee.ntu.edu.tw).

investigated by using both simulations and experiments. Particularly, effects of the low SNR of tissue harmonic signals and sound velocity inhomogeneities in the body will be studied. In addition, spatial covariance in tissue harmonic imaging will also be compared with that in linear imaging.

II. Simulation Methods and Experiment Setup

Both simulations and experiments were conducted. In the simulations, a phased array with 128 elements was assumed on both transmit and receive. The array had a pitch of 0.2 mm and a height of 7 mm. The axial focal depth was 55 mm. On transmit, non-linear propagation was simulated. The simulation model was similar to the one used by Christopher [11] and Li and Shen [14]. The model approximates continuous beam formation by incremental field propagation. Acoustic propagation of arbitrary transmit waveforms can be simulated. The transmit waveform is first decomposed into discrete temporal frequency components. At each increment, linear propagation is simulated based on the angular spectrum method [16], [17]. The nonlinear propagation is approximated based on a finite amplitude distortion model [18]. As shown in the following equation, the finite amplitude distortion model utilizes the frequency domain solution to Burgers' equation, i.e.,

$$u_n(z+\Delta z) = u'_n(z+\Delta z) + j\frac{\beta\pi f\Delta z}{2c^2}\left(\sum_{k=1}^{n-1} k u'_k u'_{n-k} + \sum_{k=n}^{N} n u'_k u'^{*}_{k-n}\right), \tag{1}$$

where z is the propagation direction and Δz is the propagation increment. The fundamental frequency is denoted by f, and β is a parameter representing the nonlinearity of the propagating medium. The term $u'_n(z+\Delta z)$ denotes the temporal velocity field at frequency nf (n is an integer) and at depth $z+\Delta z$ after linear propagation. $u_n(z+\Delta z)$ denotes the temporal velocity field after nonlinear propagation. The symbol c is sound velocity. In the simulations, the sound velocity was set to 1.54 mm/μs, and β was set to 3.5. A 2-MHz Gaussian pulse with 50% fractional bandwidth was used as the transmit waveform. The fundamental signal was extracted by a low-pass filter with a flat frequency response between dc and 3 MHz. The harmonic signal was extracted by a band pass filter with a flat frequency response between 3 and 6 MHz.

Linear propagation on receive was based on the method proposed by Li and Zagzebski [19]. The signal received by each element, $s(\vec{r},\omega)$, was computed by integrating the responses from scatterers within the region of interest to points over the entire receive transducer element. In other words, we have

$$s(\vec{r},\omega) = \int_{-b/2}^{b/2}\int_{-a/2}^{a/2} \frac{e^{jk|\vec{r}-\vec{r}'|}}{|\vec{r}-\vec{r}'|}dx'dy' \tag{2}$$

where symbol a and symbol b are the width and the height of the transducer element, respectively; $\vec{r}$ is a vector representing the position of a scatterer; $\vec{r}'$ represents a point in a transducer element; k is the wave number; and ω represents the angular frequency. Nonlinear propagation on transmit generates both fundamental and harmonic signals. The signals interact with scatterers within the region of interest and linearly propagate back to the transducer on receive. The received signals are then used for spatial covariance analysis.

Experiments were also conducted to measure spatial covariance using the experimental setup shown in Fig. 1. A gelatin-based ultrasonic phantom with uniform distribution of glass beads (Sigma G4649; Sigma Chemical Co., St. Louis, MO) was used as a speckle-generating object. An arbitrary function generator (Hewlett-Packard E1445A; Hewlett-Packard, Palo Alto, CA) was used to generate the desired transmit waveform. A power amplifier (Amplifier Research 25A250A; Souderton, PA) was used to amplify the transmit waveform and to drive a 3.5-MHz single crystal transducer (Panametrics V381; Panametrics, Waltham, MA). The transducer had an 80% −6 dB bandwidth, a diameter of 19 mm, and was geometrically focused at 70 mm.

The scattered signals were received by a separate array transducer. Setup of the transmit/receive transducers is shown graphically in Fig. 2. The two transducers were carefully aligned to ensure that signals from the focal zone of the transmitting transducer were received. Although it is different from conventional pulse-echo imaging, in which the same transducer is used for both transmit and receive, the setup shown in Fig. 2 can still be used for spatial covariance analysis without loss of generality. For linear imaging, a 5-MHz transducer array (Acuson V5; Mountain View, CA) was used. For second harmonic imaging, a 7-MHz transducer array (Acuson V7) was used. Both arrays had 128 channels, one-half-wavelength interelement spacing, and approximately an 80% fractional bandwidth. Selection of the transducer in different imaging modes was based on the respective frequency range of fundamental imaging and second harmonic imaging. A three-axis step-motor system (Q-Sync; Hsin-Chu, Taiwan, R.O.C.) was used to position the arrays such that the returning echoes could be received at different locations for spatial covariance analysis. By using the step motor system, both the linear signal and the second harmonic signal can be measured at the same positions. Note that elevational focal depths of the two arrays were both shallower than the focal depth of the transmit transducer. Thus, the effective two-way sample volume is primarily determined by the transmit sample volume because echo data were acquired near the transmit focal depth and out of the receive focal zone. The received signal was then sent to an ultrasonic receiver (Panametrics Model 5800; Waltham, MA). Finally, an analog-to-digital converter with a 20-Msamples/s sampling rate and 12-bit resolution (Hewlett-Packard E1429A) was used to sample the signal for off-line processing. The received data were up-sampled to 160 Msamples/s (i.e., 6.25-ns temporal precision) before the covariance functions

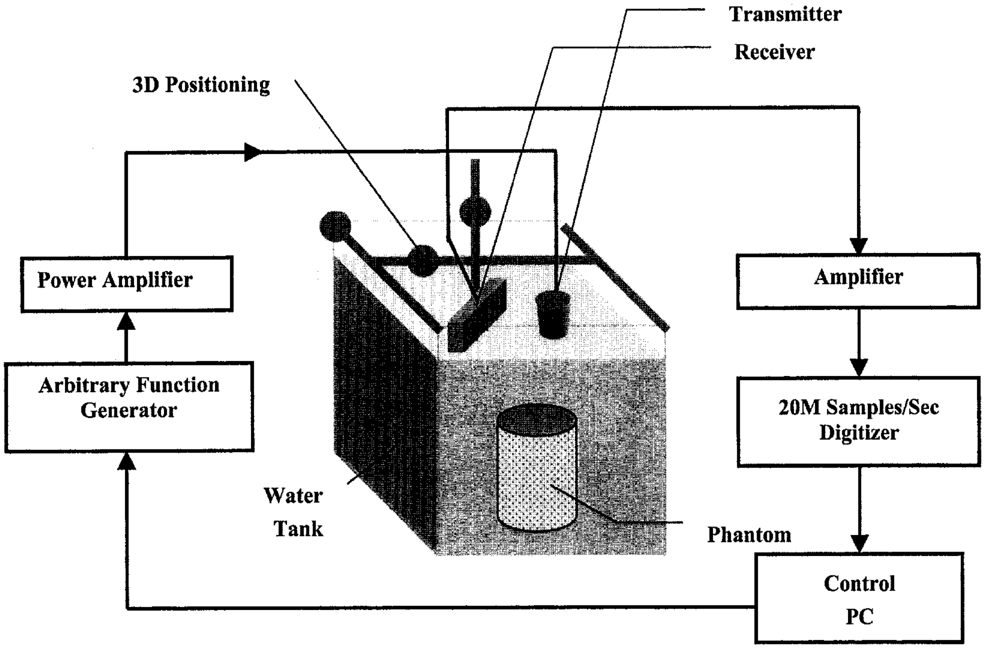

Fig. 1. Schematic diagram of the spatial covariance experimental setup.

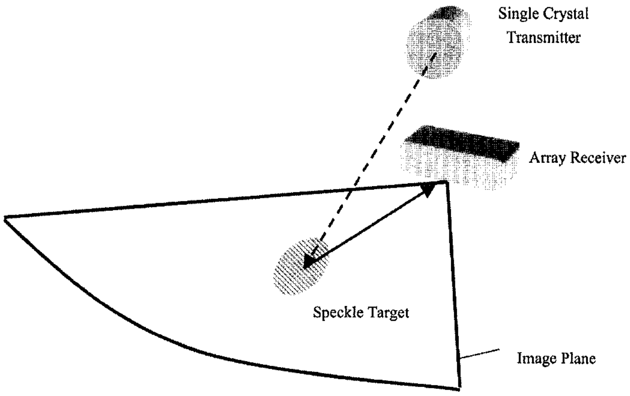

Fig. 2. Setup of the transmit and receive transducers.

were calculated. At each measurement point, the acoustic signal was acquired 16 times for signal averaging. The entire experimental setup was controlled by a Pentium-class personal computer with HP VEE software (Hewlett Packard).

III. Effects of SNR

Spatial covariance analysis in [9] assumes that the SNR is sufficiently high that the effects on spatial covariance can be ignored. In a noisy environment, however, the low SNR may affect the measured spatial covariance. In general, the covariance decreases with the SNR [20], [21]. The change in SNR has a bigger impact on the correlation results if the original SNR is lower. Because the tissue harmonic signal is typically lower than the fundamental signal by more than 20 dB [11]–[14], effects of the SNR cannot be ignored. To test this hypothesis, we investigated the spatial covariance with different SNRs.

Simulations were performed to investigate the spatial covariance in tissue harmonic imaging. The SNR was first assumed to be infinite (i.e., no noise was added in the simulations). Results are shown in Fig. 3. The horizontal axis represents the distance between two measurement positions normalized to the transmit aperture size. The vertical axis denotes normalized spatial covariance (i.e., correlation coefficient). The data window length for calculating the correlation coefficients was 2 μs for second harmonic signals and 4 μs for fundamental signals. Ten independent simulations with different scatterer distributions were used. The solid line represents average correlation coefficients for linear imaging at 2 MHz, and the dotted line denotes average second harmonic correlation coefficients at 4 MHz. Error bars represent ±1 standard deviation. As predicted by the van Cittert-Zernike theorem, spatial covariance in both cases decreases approximately linearly with the distance. This was also reported by Gauss and Trahey [22]. Nonetheless, spatial covariance in harmonic imaging is consistently lower than that in linear imaging. This is in agreement with the fact that a second harmonic beam at $2f_0$ is wider than the linear beam at twice the fundamental frequency (i.e., also at $2f_0$) [11]. Because spatial covariance and the transmit beam are a Fourier pair, spatial covariance in tissue harmonic imaging is expected to be lower than that in fundamental imaging. Thus, the linear signal is preferred for the calculating of the correlation function.

Fig. 4 and 5 demonstrate correlation coefficients at various SNRs. The SNR for linear imaging was set to be in-

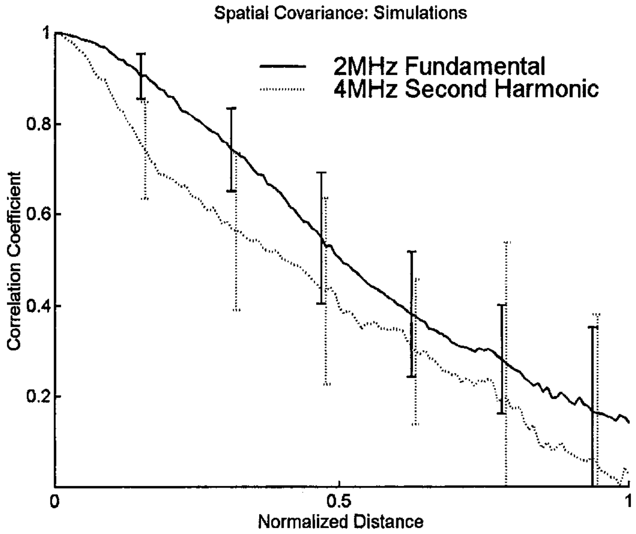

Fig. 3. Simulated spatial covariance. Solid line: 2-MHz fundamental signal; dotted line: 4-MHz second harmonic signal. Error bars indicate ±1 standard deviation.

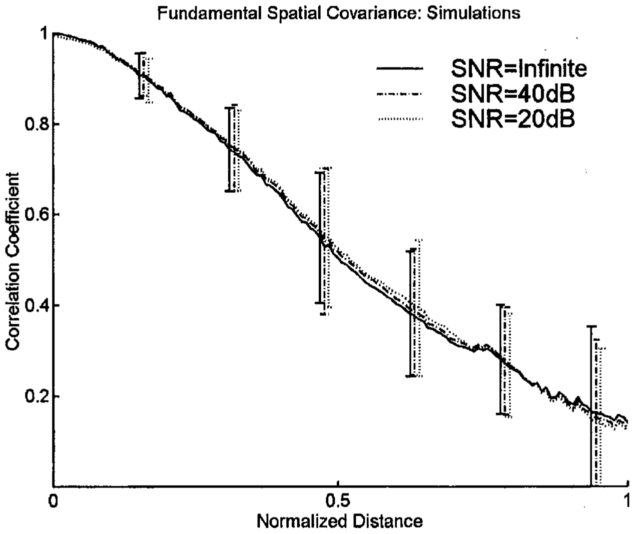

Fig. 4. Simulated spatial covariance of 2-MHz fundamental signal. Solid line: SNR = infinite; dot-dashed line: SNR = 40 dB; dotted line: SNR = 20 dB. Error bars indicate ±1 standard deviation.

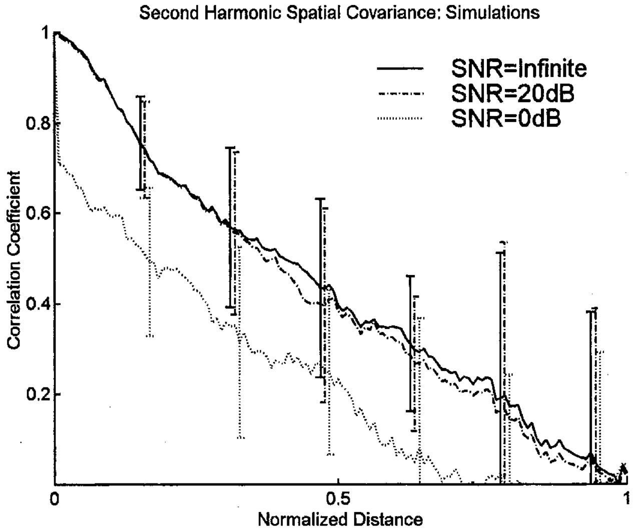

Fig. 5. Simulated spatial covariance of 4-MHz second harmonic signal. Solid line: SNR = infinite; dot-dashed line: SNR = 20 dB; dotted line: SNR = 0 dB. Error bars indicate ±1 standard deviation.

finite, 40 dB, and 20 dB. Because the second harmonic signal was 20 dB lower than the fundamental signal in the simulations, the SNR for harmonic imaging corresponded to infinite, 20 dB, and 0 dB, respectively. In both figures, results with an infinite SNR (shown by the solid lines) were the same as the two curves shown in Fig. 3. The dot-dashed lines denote an SNR of 40 dB for linear imaging and 20 dB for harmonic imaging. Similarly, the dotted lines represent an SNR of 20 dB for linear imaging and 0 dB for harmonic imaging. It is shown that spatial covariance is significantly affected at a low SNR. Because the SNR for tissue harmonic imaging is typically low, the SNR plays a more important role in tissue harmonic imaging than in fundamental imaging.

Effects of the SNR were also investigated by experiments. The SNR was varied by adjusting the peak amplitude of output of the arbitrary function generator shown in Fig. 1. The high SNR corresponded to a peak amplitude of 5 V, and the low SNR corresponded to a peak amplitude of 1 V. In both cases, the transmit waveform had a Gaussian envelope with a 3.5-MHz center frequency and a 25% fractional bandwidth. Signal processing for experimental data was similar to that for simulation data. The fundamental signal was extracted by a band-pass filter with a flat frequency response between 2.5 and 4.5 MHz. The harmonic signal was extracted by another band-pass filter with a flat frequency response between 6 and 8 MHz. The data window length for covariance analysis was 10 μs.

Fig. 6 shows the covariance function at the fundamental frequency (i.e., 3.5 MHz), and Fig. 7 shows results at the second harmonic frequency (i.e., 7 MHz). SNRs of the fundamental signals were about 35 dB (solid) and 30 dB (dotted), and the corresponding SNRs of the harmonic signals were about 20 dB (solid) and 5 dB (dotted). Fig. 6 indicates that spatial covariance was not affected by the change in SNR in linear imaging. In addition, both curves decrease from one to zero as the distance increases from zero to the transmit aperture size. However, the correlation coefficient in Fig. 7 reduces significantly when the transmit voltage changes from 5 to 1 V. This agrees with the results shown in Fig. 4 and 5. Fig. 8 redraws the high SNR results shown in Fig. 6 and 7. The solid line is for fundamental imaging, and the dotted line is for second harmonic imaging. Both curves decrease from one to zero as the distance increases from zero to the transmit aperture size. Again, the harmonic coefficients are consistently lower than the fundamental coefficients. The results agree well with the simulation results shown in Fig. 3.

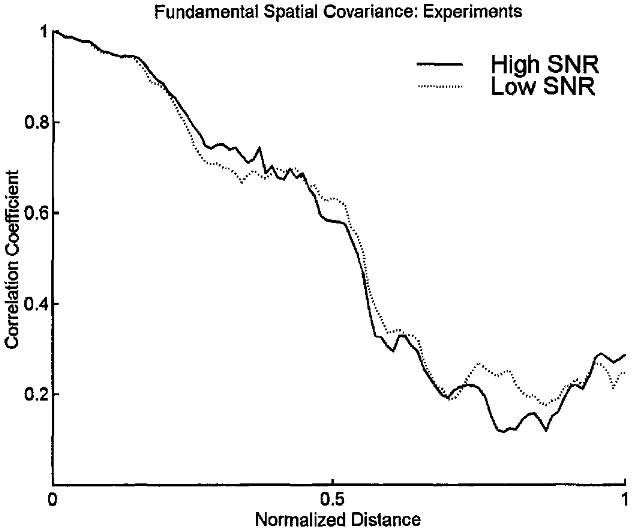

Fig. 6. Spatial covariance of 3.5-MHz fundamental signal. Solid line: high SNR; dotted line: low SNR.

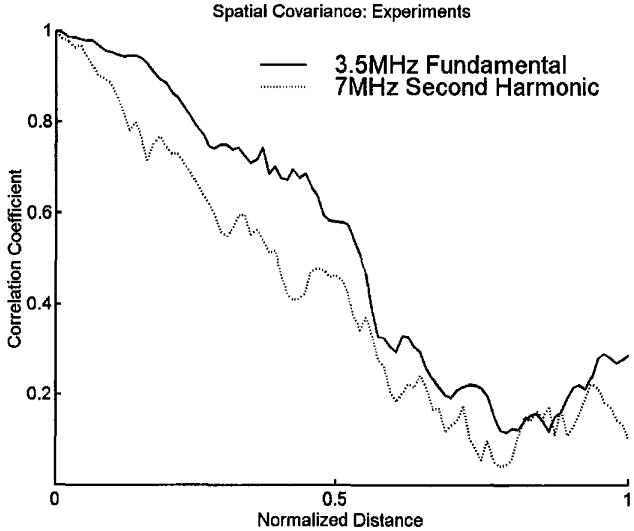

Fig. 8. Spatial covariance of 3.5-MHz fundamental signal (solid line) and 7-MHz second harmonic signal (dotted line).

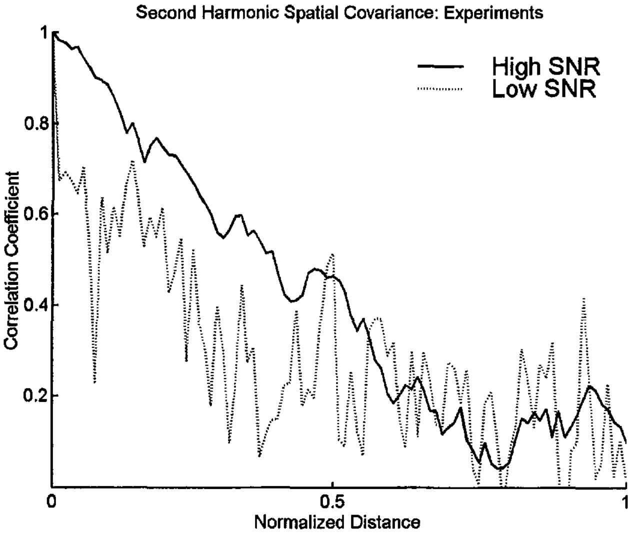

Fig. 7. Spatial covariance of 7-MHz second harmonic signal. Solid line: high SNR; dotted line: low SNR.

The signals received at different positions can also be used to form images using the synthetic aperture approach. Because the transmit aperture was fixed, the synthesized images with dynamic focusing and steering on receive can be used to evaluate the transmit beam. This is also known as the fixed direction transmit and all direction receive focusing [23], [24] or the single transmit imaging [25]. As shown in Fig. 2, the image was actually the transmit beam sliced by the receiver scan plane. The upper panel of Fig. 9(a) shows the 3.5-MHz fundamental beam using single transmit imaging over a 30-dB display dynamic range. The image is with sector scan format prior to scan conversion. The horizontal axis is the steering angle and the vertical axis represents the image range. The lower panel of Fig. 9(a) shows the lateral beam plot by projecting the pattern in the upper panel along the range direction. Fig. 9(b) shows the second harmonic beam in the same format. Note that high sidelobes are present in Fig. 9(b) because echo data were acquired out of the elevational focal region of the receive aperture. Compared with the fundamental beam pattern, the second harmonic beam has a narrower lateral beam width and a higher noise background. The narrower harmonic beam does not benefit the harmonic spatial covariance because it is still lower than the linear spatial covariance, as shown in Fig. 8. In addition, the low SNR of tissue harmonic imaging may also degrade the spatial covariance. Thus, tissue harmonic imaging does not provide any advantage over linear imaging in terms of accuracy of correlation-based time delay estimation, despite the fact that the harmonic beam is narrower than the fundamental beam.

IV. Effects of Sound Velocity Inhomogeneities

Tissue harmonic imaging is less sensitive to sound velocity variations present in the body [11], [12]. Simulations and experiments were also conducted to compare spatial covariance in the presence of sound velocity inhomogeneities. To model sound velocity variations, a displaced phase screen was included in the simulations. Such a model is similar to the one proposed by Liu and Waag [6]. Two different media were included in the simulations. The medium next to the transducer had a propagation velocity of 1.45 mm/μs, a uniform thickness of 15 mm, and a β of 6 to mimic the nonlinear properties of fat tissue [26]. The deeper medium had a propagation velocity of 1.54 mm/μs, a thickness of 65 mm, and a β of 3.5. Axial focus was at 55 mm from the transducer. Time delay errors resulting from irregular thickness of fat tissue

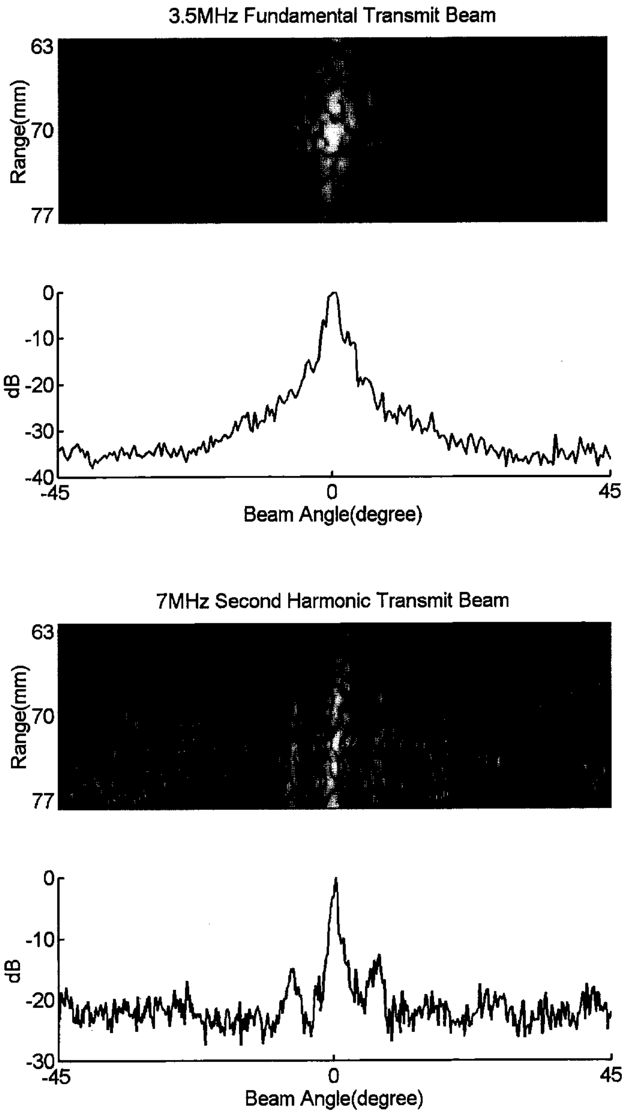

Fig. 9. a) 3.5-MHz fundamental transmit beam (top) and the projected lateral beam plot (bottom). b) 7-MHz second harmonic transmit beam (top) and the projected lateral beam plot (bottom).

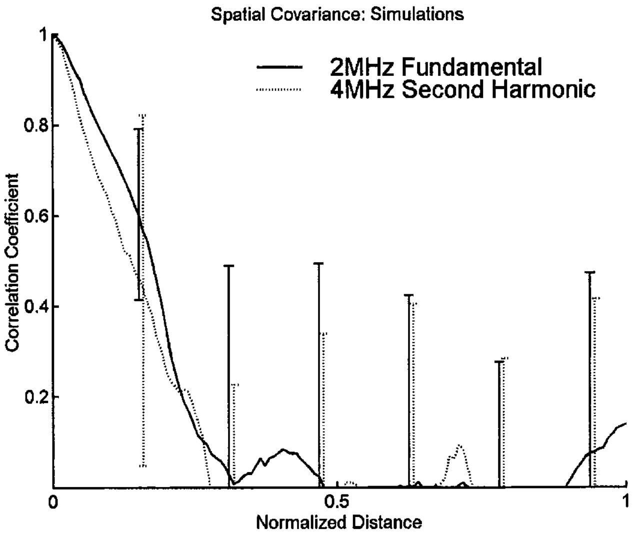

Fig. 10. Simulated spatial covariance in the presence of sound velocity inhomogeneities. Solid line: 2-MHz fundamental signal; dotted line: 4-MHz second harmonic signal. Error bars indicate ±1 standard deviation.

were simulated using a two-dimensional phase screen at the boundary of the two media. The time delay errors had a correlation length of 5 mm and a standard deviation of 93 ns. Results are shown in Fig. 10; error bars represent ±1 standard deviation. Spatial covariance decreases more rapidly for both linear imaging and harmonic imaging because of the distorted transmit beam. Similar to the results shown in Fig. 3, where sound velocity variations were absent, the harmonic covariance is generally lower than the fundamental covariance, even in the presence of sound velocity variations.

Effects of sound velocity inhomogeneities were also experimentally investigated by inserting a rubber layer (General Electric RTV511; Waterford, NY) between the transmit transducer and the gelatin phantom shown in Fig. 2. Peak amplitude of output of the function generator was set to 5 V to ensure adequate SNR for both fundamental imaging and second harmonic imaging. The rubber had a sound velocity of 1.015 mm/μs, an average thickness of 5 mm, and a correlation length of about 6 mm. Sound velocity variations were introduced by making the surface of the rubber layer irregular. The standard deviation of arrival time errors of the rubber layer was about 70 ns. Because a separate transducer was used on receive, the receive transducer was not affected by the rubber layer. Spatial covariance functions are shown in Fig. 11, and the corresponding transmit beam patterns are shown in Fig. 12. As shown in Fig. 11, the covariance decreases more rapidly than the theoretical curve because of the inserted rubber layer. Nevertheless, the fundamental spatial covariance (solid line) is generally similar to the second harmonic spatial covariance (dotted line). The second harmonic beam, shown in the lower panel of Fig. 12, is noticeably narrower than the fundamental beam, shown in the upper panel. Again, tissue harmonic imaging does not provide any advantages in terms of accuracy of correlation-based time delay estimation, despite the fact that the harmonic beam is narrower than the fundamental beam. Moreover, if aberrations are included in the receive path, the harmonic beam may be more degraded than the fundamental beam because of the higher frequency. Therefore, the linear signal is preferred for the calculation of the correlation function.

The assumption that a higher frequency linear beam is more affected by sound velocity inhomogeneities than a lower frequency linear beam was also tested. Fig. 13 shows the spatial covariance functions for linear imaging at both 3.5 and 5 MHz in the presence of sound velocity inhomogeneities. The 5-MHz array transducer was used to receive returning echoes in both cases. Because time delay errors were introduced by the same rubber layer, sound velocity inhomogeneities produced small phase errors at the lower

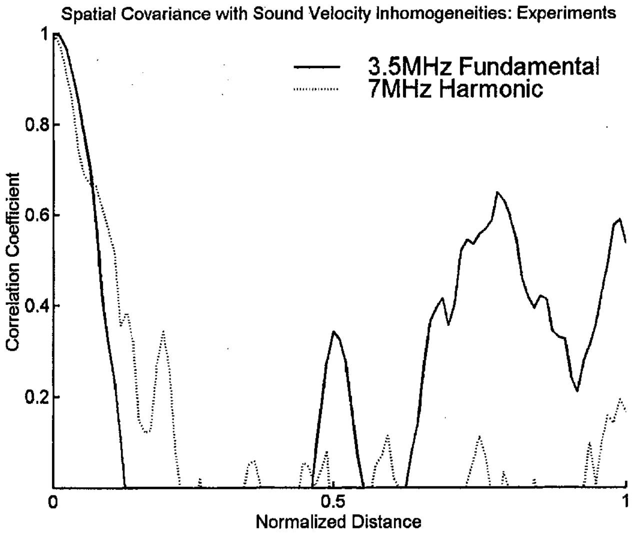

Fig. 11. Spatial covariance of 3.5-MHz fundamental signal (solid line) and 7-MHz second harmonic signal (dotted line) in the presence of sound velocity inhomogeneities.

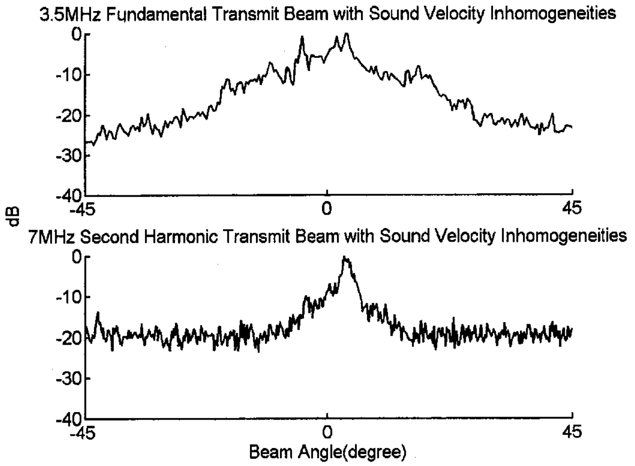

Fig. 12. Lateral beam plots of 3.5-MHz fundamental signal (top) and 7-MHz second harmonic signal (bottom) in the presence of sound velocity inhomogeneities.

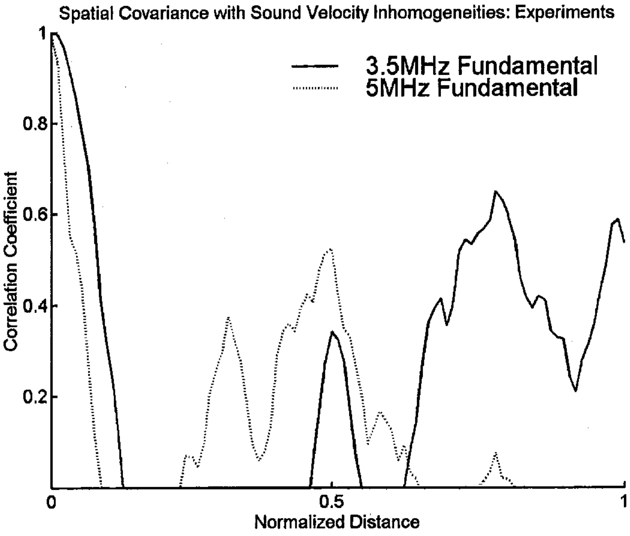

Fig. 13. Spatial covariance of 3.5-MHz fundamental signal (solid line) and 5-MHz fundamental signal (dotted line) in the presence of sound velocity inhomogeneities.

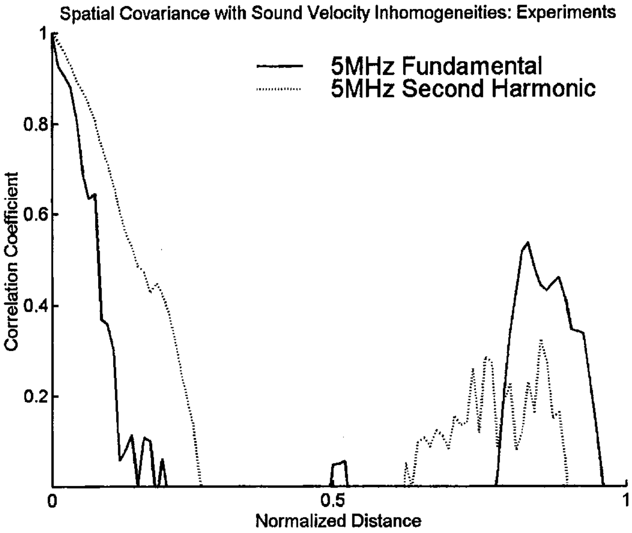

Fig. 14. Spatial covariance of 5-MHz fundamental signal (solid line) and 5-MHz second harmonic signal (dotted line) in the presence of sound velocity inhomogeneities.

frequency and larger phase errors at the higher frequency. Thus, the covariance function at 3.5 MHz declines more slowly than the 5-MHz counterpart. In other words, the lower portion of the received linear signal generally provides more accurate correlation-based estimation results.

Finally, spatial covariance of the harmonic signal and the fundamental signal received at the same frequency was evaluated in the presence of sound velocity inhomogeneities. In this case, a 2.5-MHz pulse was transmitted to obtain the second harmonic signal at 5 MHz. Another 5-MHz pulse was transmitted for the linear response. The results are compared in Fig. 14 and 15. It is shown in Fig. 14 that the 5-MHz harmonic signal (dotted line) has higher covariance than the 5-MHz fundamental signal (solid line). Because the two signals were at the same frequency, the results are consistent with the measured beam patterns shown in Fig. 15. The fundamental beam shown in the upper panel of Fig. 15 is more distorted than the second harmonic beam shown in the lower panel. Unlike the previous cases, the 5-MHz harmonic beam was generated by a 2.5-MHz fundamental beam. Because the 2.5-MHz fundamental beam is expected to be less distorted by the rubber layer than the 5-MHz fundamental beam, the 5-MHz harmonic spatial covariance is higher than the 5-MHz fundamental spatial covariance.

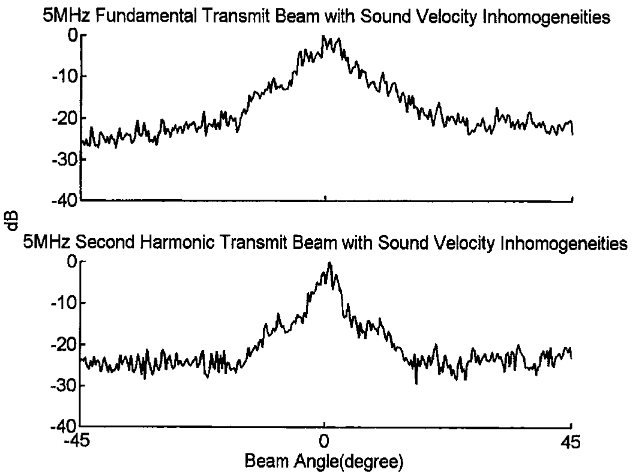

Fig. 15. Lateral beam plots of 5-MHz fundamental signal (top) and 5-MHz second harmonic signal (bottom) in the presence of sound velocity inhomogeneities.

V. CONCLUDING REMARKS

In this paper, spatial covariance under various conditions was investigated. It was shown that, if an adequate SNR is available, the spatial covariance functions at both the fundamental frequency (e.g., f_0) and the second harmonic frequency (e.g., $2f_0$) have good agreement with the prediction of the van Cittert-Zernike theorem, but the harmonic covariance is consistently lower than the fundamental covariance, with or without the presence of sound velocity variations.

At low SNRs, effects of the SNR cannot be ignored. In this case, the spatial covariance decreased, and accuracy of the correlation-based estimation may be affected. Because the SNR of tissue harmonic imaging is significantly lower than the SNR of fundamental imaging, the linear signal is preferred for correlation-based correction of sound velocity inhomogeneities. Note that both the fundamental signal at f_0 and the second harmonic signal at $2f_0$ are available for a single firing. Thus, a tissue harmonic imaging system may use the fundamental signal for correlation-based time delay estimation and the second harmonic signal for imaging.

In the presence of sound velocity inhomogeneities, performance of the correlation-based processing can be improved by using the lower frequency portion of the received linear signal. As shown in Fig. 13, the 3.5-MHz covariance is noticeably higher than the 5-MHz covariance. Thus, the lower frequency portion of a received broadband echo can be used to improve accuracy of correlation-based time delay estimation.

ACKNOWLEDGMENTS

The authors thank Acuson for providing the two arrays for the experiments. The authors also thank the reviewers for insightful comments.

REFERENCES

[1] L. M. Hinkelman and D. L. Liu, "Measurement and correction of ultrasonic pulse distortion produced by human breast," *J. Acoust. Soc. Amer.*, vol. 97, no. 3, pp. 1958–1969, Mar. 1995.

[2] L. M. Hinkelman, L. A. Metlay, and R. C. Waag, "Measurement of ultrasonic pulse arrival time and energy level variations produced by propagation through abdominal wall," *J. Acoust. Soc. Amer.*, vol. 95, no. 1, pp. 530–541, Jan. 1994.

[3] S. W. Flax and M. O'Donnell, "Phase-aberration correction using signals from point reflectors and diffuse scatterers: Basic principles," *IEEE Trans. Ultrason., Ferroelect., Freq. Contr.*, vol. 35, no. 6, pp. 758–767, Nov. 1988.

[4] M. O'Donnell and S. W. Flax, "Phase-aberration correction using signals from point reflectors and diffuse scatterers: measurements," *IEEE Trans. Ultrason., Ferroelect., Freq. Contr.*, vol. 35, no. 6, pp. 768–774, Nov. 1988.

[5] S. Krishnan, K. W. Rigby, and M. O'Donnell, "Improved estimation of phase aberration profile," *IEEE Trans. Ultrason., Ferroelect., Freq. Contr.*, vol. 44, no. 3, pp. 701–713, May 1997.

[6] D. L. Liu and R. C. Waag, "Correction of ultrasonic wavefront distortion using backpropagation and a reference waveform method for time-shift compensation," *J. Acoust. Soc. Amer.*, vol. 96, no. 2, pp. 649–659, Aug. 1994.

[7] G. C. Ng, P. D. Freiburger, W. F. Walker, and G. E. Trahey, "A speckle target adaptive imaging technique in the presence of distributed aberrations," *IEEE Trans. Ultrason., Ferroelect., Freq. Contr.*, vol. 44, no. 1, pp. 140–151, Jan. 1997.

[8] P. C. Li and M. O'Donnell, "Phase aberration correction on two-dimensional conformal arrays," *IEEE Trans. Ultrason., Ferroelect., Freq. Contr.*, vol. 42, no. 1, pp. 73–82, Jan. 1995.

[9] M. Fink and R Mallart, "The van Cittert-Zernike theorem in pulse echo measurements," *J. Acoust. Soc. Amer.*, vol. 90, no. 5, pp. 2718–2727, Nov. 1991.

[10] F. Tranquart, N. Grenier, V. Eder, and L. Pourcelot, "Clinical use of ultrasound tissue harmonic imaging," *Ultrasound Med. Biol.*, vol. 25, no. 6, pp. 889–894, 1999.

[11] T. Christopher, "Finite amplitude distortion-based inhomogeneous pulse echo ultrasonic imaging," *IEEE Trans. Ultrason., Ferroelect., Freq. Contr.*, vol. 44, no. 1, pp. 125–139, Jan. 1997.

[12] ——, "Experimental investigation of finite amplitude distortion-based second harmonic pulse echo ultrasonic imaging," *IEEE Trans. Ultrason., Ferroelect., Freq. Contr.*, vol. 45, no. 1, pp. 158–162, Jan. 1998.

[13] P.-C. Li, "Pulse compression for finite amplitude distortion based harmonic imaging using coded waveforms," *Ultrason. Imaging*, vol. 21, pp. 1–16, 1999.

[14] P.-C. Li and C.-C. Shen, "Effects of transmit focusing on finite amplitude distortion based second harmonic generation," *Ultrason. Imaging*, vol. 21, pp. 243–258, 1999.

[15] D. Langdon, G. Holley, J. Hossack, and P.-C. Li, "Ultrasonic imaging aberration correction system and method," U.S. Patent 6 023 977, Feb. 2000.

[16] D. L. Liu and R. C. Waag, "Propagation and backpropagation for ultrasonic wavefront design," *IEEE Trans. Ultrason., Ferroelect., Freq. Contr.*, vol. 44, no. 1, pp. 1–12, Jan. 1997.

[17] J. W. Goodman, *Introduction to Fourier Optics.* New York: McGraw-Hill, 1968.

[18] P. T. Christopher and K. J. Parker, "New approaches to nonlinear diffractive field propagation," *J. Acoust. Soc. Amer.*, vol. 90, no. 1, pp. 488–499, Jul. 1991.

[19] Y. Li and J. A. Zagzebski, "A frequency domain model for generating B-mode images with array transducers," *IEEE Trans. Ultrason., Ferroelect., Freq. Contr.*, vol. 46, no. 3, pp. 690–698, May 1999.

[20] B. H. Friemel, L. N. Bohs, K. R. Nightingale, and G. E. Trahey, "Speckle decorrelation due to two-dimensional flow gradients," *IEEE Trans. Ultrason., Ferroelect., Freq. Contr.*, vol. 45, pp. 317–326, 1998.

[21] W. F. Walker and G. E. Trahey, "A fundamental limit on delay estimation using partially correlated speckle signals," *IEEE Trans. Ultrason., Ferroelect., Freq. Contr.*, vol. 42, no. 2, pp. 301–308, Mar. 1995.

[22] R. C. Gauss and G. E. Trahey, "Adaptive imaging in the thyroid using fundamental and harmonic echo data," in *Proc. 1999 IEEE Ultrason. Symp.*, pp. 1515–1519.

[23] P.-C. Li, S. W. Flax, E. S. Ebbini, and M. O'Donnell, "Blocked element compensation in phased array imaging," *IEEE Trans. Ultrason., Ferroelect., Freq. Contr.*, vol. UFFC-40, no. 4, pp. 283–292, Jul. 1993.

[24] P.-C. Li and M. O'Donnell, "Improved detectability with blocked element compensation," *Ultrason. Imaging*, vol. 16, pp. 1–18, 1994.

[25] D.-L. Liu, P. V. Behren, and J. Kim, "Single transmit imaging," in *Proc. 1999 Int. Ultrason. Symp.*, pp. 1275–1278.

[26] W. K. Law, L. A. Frizzell, and F. Dunn, "Determination of the nonlinearity parameter B/A of biological media," *Ultrasound Med. Biol.*, vol. 11, no. 2, pp. 307–318, 1985.

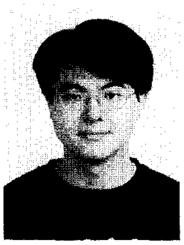

Che-Chou Shen was born in 1976 in Taiwan, R.O.C. He graduated from the Department of Electrical Engineering at National Taiwan University in 1998. He is now a graduate student working on ultrasonic harmonic imaging under the instruction of Professor P.-C. Li.

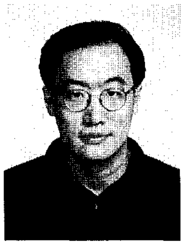

Pai-Chi Li (S'93–M'95–SM'01) received the B.S. degree in electrical engineering from National Taiwan University, Taipei, Taiwan, R.O.C., in 1987 and the M.S. and Ph.D. degrees from the University of Michigan, Ann Arbor, in 1990 and 1994, respectively, both in electrical engineering: systems.

He was a research assistant with the Department of Electrical Engineering and Computer Science from 1990 to 1994. He joined Acuson Corporation, Mountain View, CA, as a member of the Technical Staff in June 1994. His work in Acuson was primarily in the areas of medical ultrasonic imaging system design for both cardiology and general imaging applications. In August 1997, he went back to the Department of Electrical Engineering at National Taiwan University as an assistant professor. He became an associate professor in August 1998. His current research interests include biomedical ultrasonic imaging and signal processing.

Dr. Li is a senior member of IEEE, and he was the recipient of the Distinguished Achievement Award in Electrical Engineering: Systems for his outstanding academic achievement at the University of Michigan.